

NASA Technical Memorandum **100579**

**FLUID-THERMAL-STRUCTURAL STUDY OF  
AERODYNAMICALLY HEATED LEADING  
EDGES**

(NASA-TM-100579) FLUID-THERMAL-STRUCTURAL  
STUDY OF AERODYNAMICALLY HEATED LEADING  
EDGES (NASA) 16 p

CSCL 20K

N88-20666

Unclassified  
G3/39 0134766

**PRAMOTE DECHAUMPHAI, EARL A. THORNTON,  
AND ALLAN R. WIETING**

**APRIL 1988**



**Langley Research Center**  
Hampton, Virginia 23665

# FLUID-THERMAL-STRUCTURAL STUDY OF AERODYNAMICALLY HEATED LEADING EDGES

Pramote Dechaumphai\*  
NASA Langley Research Center  
Hampton, Virginia

Earl A. Thornton\*\*  
Old Dominion University  
Norfolk, Virginia

Allan R. Wieting\*\*\*  
NASA Langley Research Center  
Hampton, Virginia

## Abstract

A finite element approach for integrated fluid-thermal-structural analysis of aerodynamically heated leading edges is presented. The Navier-Stokes equations for high speed compressible flow, the energy equation, and the quasi-static equilibrium equations for the leading edge are solved using a single finite element approach in one integrated, vectorized computer program called LIFTS. The fluid-thermal-structural coupling is studied for Mach 6.47 flow over a 3-inch diameter cylinder for which the flow behavior and the aerothermal loads are calibrated by experimental data. Issues of the thermal-structural response are studied for hydrogen cooled, super thermal conducting leading edges subjected to intense aerodynamic heating.

## Nomenclature

A	coolant passage area, eq. (5), or finite element area, eq. (11)	P	coolant passage perimeter
c	specific heat, eqs. (4) and (5) or fictitious damping constant, eq. (7)	p	pressure
E,F	x and y flux components	q	heat flux
H	load vector, eq. (5)	{R}	load vector
h	convective heat transfer coefficient	T	temperature
k	thermal conductivity	T <sub>0</sub>	reference temperature for zero stress
l, m	components of unit normal vector	T <sub>∞</sub>	surrounding medium temperature
m̄	coolant mass flow rate	t	time
[M]	mass matrix	Δt	time step
[N]	element interpolation function	U	conservation variable
		u, v	flow velocity components, eq. (2), or displacement components, eq. (7)
		x, y	coordinate directions
		ρ	density
		ε	flow total energy, eq. (2), or strain components, eq. (18), or emissivity, eq. (19)
		σ	Stefan-Boltzmann constant
		σ <sub>x</sub> , σ <sub>y</sub> , τ <sub>xy</sub>	fluid stress components, eq. (2), or solid stress components, eq. (7)
		Subscripts	
		F	fluid
		T	thermal
		s	structural
		Superscript	
		n	time step index

\*Aerospace Technologist, Aerothermal Loads Branch, Loads and Aeroelasticity Division, Member AIAA

\*\*Professor, Department of Mechanical Engineering and Mechanics, Associate Fellow AIAA

\*\*\*Head, Aerothermal Loads Branch, Loads and Aeroelasticity Division, Member AIAA

## Introduction

Design of lightweight structures and thermal protection systems for hypersonic cruise and reentry vehicles depends on accurate prediction of the aerothermal loads, structural temperatures and their gradients, and the structural deformations and stresses. Traditionally, an aerodynamicist will predict the surface pressures and heating rates assuming a rigid isothermal body. These aerodynamic heating rates are used by a structural heat transfer analyst to predict the structural temperature distribution. Finally, a structural analyst uses the temperature distribution and aerodynamic pressures to predict the structural deformations and stresses. Such traditional independent approaches require several iterations between the different analysis methods and analysts. The approach is relatively inefficient because the incompatible mathematical models require extensive postprocessing to transfer data. Moreover, the interdisciplinary coupling and interactions, which are not insignificant, are rarely attempted because the iterative process not only requires several additional solutions but also remodeling in each analysis. The coupling occurs primarily through the thermal response of the structure because: (1) the surface temperature affects the external flow by changing the amount of energy absorbed by the structure, and (2) the temperature gradients in the structure result in structural deformations which alter the aerodynamic surface and hence the flow field and attendant surface pressures and heating rates. Hence, an integrated interdisciplinary analysis procedure that would provide accurate, timely prediction of the coupled response is highly desirable.

The interdisciplinary coupling and interaction has been demonstrated in the design of high speed vehicle structures. One such structure, a metallic Thermal Protection System (TPS) panel<sup>1</sup> for reentry vehicles, thermally bows into the airstream to relieve thermal stresses. The bowing creates an aerodynamic surface consisting of arrays of spherical like protuberances. As a first step to understanding the effect of the structural deformation on a hypersonic flow field caused by the interactions, the aerothermal loads on a dome surface in a Mach 6.5 stream were predicted computationally<sup>2</sup> and measured experimentally<sup>3</sup>. These studies showed that the dome configuration caused complex shock and expansion waves and attendant localized heating rates that were 2 to 6 times higher than those for a uniform flat surface. The existence of the high localized heating rates indicates that several more iterations between interdisciplinary analyses would be required to converge the aerothermostructural response of the TPS. Typically, these additional calculations were never performed.

To further understand the coupled fluid-thermal-structural interactions, a thin panel representing a typical sidewall of an actively cooled engine structure has been analyzed with an integrated fluid-thermal-structural procedure<sup>4,5</sup>. The coupled analysis showed that the aerodynamic flow field was altered: (1) as the initial uniform wall temperature became nonlinear, and

(2) as the panel deformed. The nonlinear temperature distribution and panel deformation not only changed the stress distribution in the panel, but also induced a complex external flow phenomena consisting of separated flow with shocks and flow expansions. The study confirmed that the interactions of the flow behavior, the panel temperature, and the panel deformation should not be neglected and that the interactions between the three disciplines could be coupled into a single analysis method.

Leading edges for hypersonic vehicles that experience intense stagnation point pressures and heating rates are often a challenge to the designer. For engine leading edges, such as cowls or the fuel injection strut shown in Fig. 1, the intense loads can be amplified by an order of magnitude<sup>6</sup> when the leading edge bow shock is impinged upon by an oblique shock wave. The intense localized heating causes severe temperature levels and gradients. This makes the analytical prediction difficult because of the strong nonlinearity that is present in all phases of the thermal and structural analyses. The strong nonlinearity raises uncertainty in applying the existing analysis approach to such highly nonlinear thermal-structural problems. However, nonlinear behavior is important in the design of a viable structure under such severe conditions, hence the requirements of such an analysis procedure needs to be better defined.

The purposes of this paper are to: (1) study the coupled fluid-thermal-structural behavior for aerodynamically heated leading edges using the technique developed for the heated panels, and (2) identify the critical issues or requirements for integrated fluid-thermal-structural analysis. The solution of the Navier-Stokes equations for predicting aerodynamic heating and the solution for the associated thermal-structural equations are obtained using a Taylor-Galerkin algorithm in one integrated, vectorized computer program called LIFTS (the Langley Integrated Fluid Thermal Structural analyzer).

The fluid-thermal-structural formulation used in LIFTS and the solution approach are described. The integrated analysis will be demonstrated on a three inch diameter cylinder used to obtain the experimental pressures and heat transfer rates to which the predictions will be compared. The issues associated with nonlinear thermal-structural response due to intense aerodynamic heating will be demonstrated by studies of a hydrogen cooled leading edge subjected to shock wave interference heating. The latter example will include the issues associated with the effects of severe temperature gradients on material property variations and thermal stresses.

## Fluid-Thermal-Structural Formulation

### Aerodynamic Flow

The equations for aerodynamic flow are described by the conservation of mass, momentum, and energy equations. These equations can be written in the conservation form

$$\frac{\partial}{\partial t} (U_F) + \frac{\partial}{\partial x} (E_F) + \frac{\partial}{\partial y} (F_F) = 0 \quad (1)$$

where the subscript F denotes the flow analysis,  $\{U_F\}$  is the vector of the conservation variables;  $\{E_F\}$  and  $\{F_F\}$  are vectors of the flux components in the x and y directions. These vectors are given by

$$\begin{aligned} \{U_F\}^T &= [\rho \quad \rho u \quad \rho v \quad \rho e \quad] \\ \{E_F\}^T &= [\rho u \quad \rho u^2 + p \quad \rho uv \quad \rho ue + pu \quad] \\ &\quad - [0 \quad \sigma_x \quad \tau_{xy} \quad u\sigma_x + v\tau_{xy} - q_x] \\ \{F_F\}^T &= [\rho v \quad \rho uv \quad \rho v^2 + p \quad \rho ve + pv \quad] \\ &\quad - [0 \quad \tau_{xy} \quad \sigma_y \quad u\tau_{xy} + v\sigma_y - q_y] \end{aligned} \quad (2)$$

where  $\rho$  is the fluid density,  $u$  and  $v$  are velocity components, and  $e$  is the total energy. Each of the flux vectors contains two vectors of flux components representing the inviscid and viscous flux components. In the inviscid flux components, the pressure  $p$  is related to the total energy assuming a calorically perfect gas (constant ratio of specific heats). In the viscous flux components, the stresses  $\sigma_x$ ,  $\sigma_y$ , and  $\tau_{xy}$  are related to the velocity gradients assuming Stokes' hypothesis<sup>7</sup>. The heat fluxes  $q_x$  and  $q_y$  are related to the temperature gradients by Fourier's law. The temperature-dependent viscosity is computed from Sutherland's law<sup>7</sup> and the thermal conductivity is computed assuming a constant Prandtl number of 0.72.

### Structural Heat Transfer

The thermal response of the structure is described by the energy equation which can be written in conservation form

$$\frac{\partial}{\partial t} (U_T) + \frac{\partial}{\partial x} (E_T) + \frac{\partial}{\partial y} (F_T) = H_T \quad (3)$$

where the subscript T denotes the thermal analysis,  $U_T$  is the conservation variable,  $E_T$  and  $F_T$  are the flux components, and  $H_T$  is the heat load. For transient heat conduction without internal heat source, these quantities are

$$\begin{aligned} U_T &= \rho_s c_s T_s \\ E_T &= q_x \\ F_T &= q_y \\ H_T &= 0 \end{aligned} \quad (4)$$

where  $\rho_s$  is the material density,  $c_s$  is the material specific heat, and  $T_s$  is the temperature. The heat fluxes  $q_x$  and  $q_y$  are related to temperature gradients by Fourier's law.

For a convectively cooled structure, the thermal mass transport by the coolant is prescribed by an energy conservation equation based on: (1) a bulk

coolant temperature, (2) a convective heat transfer coefficient that represents the thermal conductance between the structure and the coolant, and (3) the coolant mass flow rate<sup>8</sup>. The energy equation for the coolant flow in the local x direction can be written in the form of eq. (3) where

$$\begin{aligned} U_T &= \rho_f c_f T_f \\ E_T &= \dot{m} c_f T_f / A_f - k_f \partial T_f / \partial x \\ F_T &= 0 \\ H_T &= h P (T_s - T_f) \end{aligned} \quad (5)$$

In this equation,  $\rho_f$  is the coolant density,  $c_f$  is the coolant specific heat,  $T_f$  is the coolant bulk temperature,  $\dot{m}$  is the coolant mass flow rate, and  $k_f$  is the coolant thermal conductivity. Therefore,  $E_T$  consists of the energy transport by convection (1st term) and conduction (2nd term), and  $H_T$  represents the heat transfer between the structure and the coolant.

### Structural Response

The structural response is described by the quasi-static equations of motion which can be written in conservation form

$$\frac{\partial}{\partial t} (U_s) + \frac{\partial}{\partial x} (E_s) + \frac{\partial}{\partial y} (F_s) = 0 \quad (6)$$

where the subscript s denotes the structural analysis,  $\{U_s\}$  is the displacement vector;  $\{E_s\}$  and  $\{F_s\}$  are vectors of the stress components and are given by

$$\begin{aligned} \{U_s\}^T &= [cu \quad cv] \\ \{E_s\}^T &= [-\sigma_x \quad -\tau_{xy}] \\ \{F_s\}^T &= [-\tau_{xy} \quad -\sigma_y] \end{aligned} \quad (7)$$

where  $u$  and  $v$  are displacement components in the x and y directions respectively;  $c$  is a pseudo-damping constant used to facilitate marching to a steady-state quasi-static solution. The panel stress components  $\sigma_x$ ,  $\sigma_y$ , and  $\tau_{xy}$  are related to the displacement gradients and the temperature by the generalized Hooke's law.

### Solution Procedure

An explicit time marching finite element scheme, the Taylor-Galerkin algorithm, described in Refs. [4-5] is used to solve the fluid thermal structural equations (1) - (7). For brevity, only the essential features of the algorithm are highlighted herein.

### Taylor-Galerkin Algorithm

The basic concept of the Taylor-Galerkin algorithm is to use: (1) Taylor series expansion in time to

establish recurrence relations for time marching, and (2) the method of weighted residuals with Galerkin's criterion for spatial discretization. The fluid, thermal, and structural conservation equations are written in the form of a scalar equation,

$$\frac{\partial U}{\partial t} + \frac{\partial E}{\partial x} + \frac{\partial F}{\partial y} = 0 \quad (8)$$

The key feature of the algorithm is to express the variation of the element fluxes  $E$  and  $F$  in the same form as the element dependent variable  $U$ , that is

$$\begin{aligned} U(x, y, t) &= [N(x, y)]\{U(t)\} \\ E(x, y, t) &= [N(x, y)]\{E(t)\} \\ F(x, y, t) &= [N(x, y)]\{F(t)\} \end{aligned} \quad (9)$$

where  $[N(x, y)]$  denotes the element interpolation functions, and  $\{U\}$ ,  $\{E\}$ , and  $\{F\}$  are the vectors of the element nodal quantities.

For flow analysis, the computation proceeds through two time levels,  $t_{n+1/2}$  and  $t_{n+1}$ . At time level  $t_{n+1/2}$ , values of  $U$  are assumed constant within each element. At time level  $t_{n+1}$ , the nodal values of  $U$  are computed assuming a linear element variation. The final equations are in the form,

$$[M] \{ \Delta U_F \}^{n+1} = \{ R_F \}_1^n + \{ R_F \}_2^n + \{ R_F \}_3^{n+1/2} \quad (10)$$

where  $\Delta U^{n+1} = U^{n+1} - U^n$  and  $[M]$  denotes the mass matrix,

$$[M] = \int_A [N] [N] dA \quad (11)$$

The first two vectors on the right hand side of eq. (10) represent the viscous flux over the element area and along the element boundary,

$$\begin{aligned} \{ R_F \}_1^n &= -\Delta t \left( \int_A \left( \frac{\partial N}{\partial x} \right) [N] dA \{ E \}^n \right. \\ &\quad \left. + \int_A \left( \frac{\partial N}{\partial y} \right) [N] dA \{ F \}^n \right) \end{aligned} \quad (12)$$

$$\{ R_F \}_2^n = \Delta t \int_S [N] [N] ds (l \{ E \}^n + m \{ F \}^n) \quad (13)$$

where  $\Delta t$  is the timestep and the coefficients  $l$  and  $m$  are the components of a unit vector normal to the boundary. The last vector on the right hand side of eq. (10) represents both the inviscid and viscous fluxes evaluated at time level  $t_{n+1/2}$ . All matrices in eqs. (11) - (13) are evaluated in closed form<sup>9</sup>. To produce an explicit algorithm, the mass matrix  $[M]$  in eq. (11) is diagonalized.

For thermal analysis, a single time level version of the algorithm is used<sup>10</sup>. Derivation of the element equations proceeds in the same fashion as described for the flow analysis. The final element equations are in the form,

$$[M] \{ \Delta U_T \}^{n+1} = \{ R_T \}_1^n + \{ R_T \}_2^n \quad (14)$$

where

$$\begin{aligned} \{ R_T \}_1^n &= \Delta t \left( \int_A \left( \frac{\partial N}{\partial x} \right) [N] dA \{ E_T \}^n \right. \\ &\quad \left. + \int_A \left( \frac{\partial N}{\partial y} \right) [N] dA \{ F_T \}^n \right) \end{aligned} \quad (15)$$

$$\begin{aligned} \{ R_T \}_2^n &= -\Delta t \int_S [N] [N] dS (l \{ E_T \}^n + m \{ F_T \}^n) \\ &= -\Delta t \int_S [N] [N] dS \{ q \}^n \end{aligned} \quad (16)$$

The vectors  $\{E_T\}$  and  $\{F_T\}$  contain the element nodal heat flux components. The vector  $\{q\}$  in eq. (16) represents nodal heat fluxes normal to the element surface boundary. Typical nodal heat flux components, for an isotropic material as an example, are computed from Fourier's law,

$$\begin{aligned} E_T &= q_x = -k(T) \frac{\partial T}{\partial x} \\ F_T &= q_y = -k(T) \frac{\partial T}{\partial y} \end{aligned} \quad (17)$$

The nodal temperature gradients  $\partial T / \partial x$  and  $\partial T / \partial y$  depend on element types and element nodal temperatures, and can be computed explicitly. Benefits of the Taylor-Galerkin algorithm include: (1) all element matrices and element nodal quantities can be evaluated in closed form, i.e., numerical integration is not required, even for quadrilateral elements, (2) material nonlinearity such as temperature dependent thermal conductivity can be included directly (eq. (17)), (3) nonlinear boundary conditions which will be described in the subsequent section can be implemented easily, and (4) an explicit time marching scheme can be used for transient nonlinear analysis, if preferred, thus avoiding the iterative solution of a set of simultaneous equations.

The same approach used for the thermal analysis is applied to derive the finite element equations for the structural analysis<sup>10</sup>. The equations are identical to eqs. (14) to (16) except that the subscript  $T$  is replaced by the subscript  $s$  everywhere. The vectors  $\{E_s\}$  and  $\{F_s\}$  now represent the element nodal stress components. For an elastic orthotropic material, typical nodal stress components in two dimensions are obtained using constitutive relations,

$$\sigma_i = c_{ij} \epsilon_j + \beta_i (T - T_o) \quad i, j = 1, 2, 3 \quad (18)$$

where  $T_0$  is the reference temperature for zero thermal stress. The material elastic constants  $c_{ij}$  and the thermal expansion parameters  $\beta_i$  may be temperature dependent. Large-strain displacement relations are available in LIFTS and can be included in the computation of the strain components  $\epsilon_j$ .

The explicit Taylor-Galerkin procedure described herein is conditionally stable. The allowable time steps depend on the size of elements and the characteristics of the problem. Guidelines for determining allowable time steps have been established and can be found in Refs. 10-11.

### Initial and Boundary Conditions

The fluid, thermal, and structural eqs. (1), (3), and (6) are solved subject to appropriate initial and boundary conditions. The initial conditions for these problems consist of specifying the distributions of the conservation variables {U} at time zero.

The boundary conditions for supersonic flow consist of specifying all conservation variables along the in-flow surfaces. On supersonic outflow surfaces, the finite element formulation provides appropriate boundary conditions. A no slip condition (velocities set to zero) is specified at the solid surface.

The boundary conditions for the thermal analysis are applied via the vector shown in eq. (14) and expressed in eq. (16). The surface nodal heat flux  $q$  is replaced by the quantities representing different types of thermal boundary conditions,

$$q = \begin{cases} 0 & (\text{insulated}) \\ q_s & (\text{specified heating}) \\ h(T_s - T_\infty) & (\text{surface convection}) \\ \epsilon\sigma(T_s^4 - T_\infty^4) & (\text{surface radiation}) \end{cases} \quad (19)$$

The boundary conditions for the structural analysis, such as the applied pressure, can be added into the structural equations via the surface boundary vector. The procedure is identical to that for the thermal analysis previously described and is therefore omitted.

For fully integrated analysis, the aerodynamic pressure and surface heating rate are integral parts of the analysis and are not boundary conditions. The Taylor-Galerkin approach permits the different disciplines to be combined easily for the coupled analysis. As an example, the coupled solution for the flow and the structure temperature can be obtained by solving the equation that combines the flow energy eq. (10) and the structure energy eq. (14). The result contains an interface temperature distribution valid for both the flow field and the structure and provides the continuity of heat flux across the boundary.

### Applications

Two applications are presented to study the fluid-thermal-structural behavior of aerodynamically heated leading edges. A three inch diameter stainless steel cylinder subjected to aerodynamic heating from a Mach 6.47 flow is used as the first example to demonstrate the integrated analysis and validate predicted surface pressure and heating rates with experiment. The second example is a study of the thermal-structural response of a 0.25 inch diameter hydrogen cooled leading edge subjected to intense shock wave interference heating. Critical issues for integrated fluid-thermal-structural analysis and design of the leading edges are identified.

### Mach 6.47 Flow Over a Cylinder

The solution to Mach 6.47 flow over a cylinder is used to demonstrate the integrated flow-thermal-structural analysis approach and validate the analytical prediction of the aero-thermal loads. A schematic of the experiment, performed in the NASA Langley 8-foot High Temperature Tunnel, is shown in Fig. 2. A 3-inch diameter, 0.5 inch thick, stainless steel cylinder was mounted on the panel holder and subjected to a uniform high enthalpy Mach 6.47 flow. Approximately 50 pressure taps and coaxial thermocouples were placed circumferentially along the cylinder surface to accurately determine the aerodynamic pressure and heating rate distribution. Details of the experimental configurations, the tunnel flow conditions, and the experimental results are given in Ref. 6.

The finite element model representing the flow domain and the cylinder is shown in Fig. 3. Due to symmetry, only one-half of the incoming flow domain and one-fourth of the cylinder are modeled. The flow field is characterized by the bow shock that stands off the cylinder and the thin boundary layer at the cylinder surface. Sharp gradients in the flow variables occur in these regions, hence closely spaced elements are required for resolution. In the remaining area between the body and bow shock, flow gradients are significantly smaller hence element spacing can be larger. Since the flow structure is known apriori the flow field mesh is constructed to space elements closely together in the shock region and boundary layer. The elements are also densely packed along the stagnation line ( $y=0$ ). In this region close to the cylinder surface, the flow velocities are very small and become zero at the stagnation point. Away from the flow symmetry line, the subsonic flow accelerates nonuniformly to sonic speeds.

The finite element model consists of 12,000 quadrilateral elements in the flow domain and 3,000 quadrilateral elements for the cylinder with the same discretization along the flow-cylinder interface. A graded radial spacing was used in the cylinder. About 35% of the fluid elements lie in the 0.02 inch thick boundary layer. The boundary layer mesh is graduated normal to the cylinder surface by an incremental factor of 1.1. The smallest element is at the flow stagnation point and is only 0.0004 inch long

in the direction normal to the cylinder surface. This extremely small element dimension is necessary to capture the temperature gradient and hence the aerodynamic heating rate.

Typical flow solutions are shown in Figs. 4-7. Predicted density contours are compared in Fig. 4 with an experimental schlieren photograph<sup>6</sup> which is also a measure of flow density. The comparison of the shock shape and position indicates the global flow field is reasonably well predicted. Fig. 5 shows the excellent agreement between the computed aerodynamic pressure distribution along the cylinder surface and the experimental data<sup>6</sup>. The predicted and experimental pressures are normalized by their respective stagnation point pressures which were within 5% of each other.

The major difficulty in the fluid analysis is the prediction of the aerodynamic heating rates because a very accurate resolution of the flow temperature gradient normal to the cylinder surface is required. The computed flow temperature distribution (Fig. 6) along the flow symmetry line ( $y=0$ ) clearly illustrates the sharp gradients that must be resolved. The free-stream temperature increases abruptly from 435°R to about 3,900°R across the bow shock. Within a very thin layer at the flow stagnation point, the temperature drops sharply from 3,900°R to the surface temperature of 530°R. This steep temperature gradient within the thin layer, which is about 3% of the shock layer thickness, produces a high stagnation point heating rate. The predicted bow shock location compares well with the location predicted by empirical formulae<sup>12</sup> and the schlieren photograph (Fig. 4). The predicted heating rate distribution normalized to the stagnation point heating rate at time zero compares well with the experimental results<sup>6</sup> as shown in Fig. 7. The predicted stagnation point heating rate (42.5 Btu/ft<sup>2</sup>-sec) is in excellent agreement with the Fay and Riddell solution<sup>13</sup> (42.5 Btu/ft<sup>2</sup>-sec) and a viscous shock layer solution<sup>14</sup> (41.4 Btu/ft<sup>2</sup>-sec) but is quite lower than the experiment<sup>6</sup> (61.7 Btu/ft<sup>2</sup>-sec). The difference between the predicted and the experimental heating rate has not been resolved, but it could result from high temperature effects not taken into account by the analysis or from free stream turbulence in the test stream.

Since the flow field reaches equilibrium instantaneously compared to the thermal response of the cylinder, this aerodynamic analysis was updated at two second intervals. The cylinder temperature contours at two seconds are shown in Fig. 8. The figure shows the maximum temperature of about 700°R occurs at the stagnation point whereas the temperature along the back side of the cylinder remains at the ambient temperature of 530°R. The structure responds instantly to the pressure and temperature field hence a quasi-static structural analysis is adequate to predict the cylinder deformations and thermal stresses. The structural boundary conditions and the resulting circumferential thermal stress distribution on the cylinder are shown in Fig. 9. A maximum compressive stress of 32 ksi occurs

on the cylinder outer surface near the stagnation point due to the high temperature gradients in that region. The cylinder deformation is negligible compared to the cylinder diameter due to the relatively low temperature change and hence has a negligible effect on the aerodynamic flow. However, the change in the surface temperature has a moderate effect on the flow field. The aerodynamic heating rate is reduced in the region where the surface temperature has increased as shown in Fig. 7, due to a thickening of the thermal boundary layer and a lower fluid temperature gradient at the cylinder surface. The stagnation point heating rate decreased nearly 8% from the initial level with the cylinder temperature at 530°R.

The coupling in this problem is moderate to weak and occurs primarily between the flow and thermal analyses. Since the flow and stress fields are not coupled and develop instantaneously compared to the structural temperature field, an iterative solution between disciplinary solutions would be adequate. Of course, the integrated analysis significantly eased data transfer between disciplinary analyses.

A major difficulty encountered in the flow field solution was the convergence of the aerodynamic heating rate. The aerodynamic heating rate, especially in the flow stagnation zone, converged slowly because the small mesh needed to capture the high temperature gradient required a very small time step to satisfy the computational stability criterion. Hence, coupled with low flow velocities, perturbations take a large number of time steps to convect out of the flow domain.

To increase the convergence rate of the aerodynamic heating and reduce the analysis computational time, the current analysis approach must be modified. This may be done by applying an implicit solution technique for the flow boundary layer region to alleviate the computational stability constraint and thus increase the convergence rate. The computational intensity can be further reduced by reducing the number of unknowns (i.e. grid points and elements). This is achieved by adapting the computational domain to the physics of the phenomena creating an unstructured computational domain.

These modifications were developed recently at the Aerothermal Loads Branch, NASA Langley Research Center, in a program called LARCNESS<sup>15</sup> (Langley Adaptive Remeshing Code and Navier-Stokes Solver). The approach employs an implicit/explicit upwind finite element algorithm combined with an adaptive unstructured mesh refinement technique. The approach has been applied with excellent results to the flow problems described herein<sup>15</sup>. To demonstrate an application of the adaptive unstructured mesh refinement technique, a more complex flow behavior representing the second example where an oblique shock intersects the cylinder bow shock is described in Fig. 10(a). The intersection creates a supersonic jet that impinges on the cylinder<sup>6</sup>. The adaptive unstructured finite element model is shown in Fig. 10(b). The elements are

adaptively clustered to accurately capture the shock interaction phenomena and the flow solution in the boundary layer. The adaptive procedure, based on density gradients in the flow field, significantly reduced the number of grid points. This more complex flow field was resolved with 9000 grid points compared to 12000 grid points used in this study for the simpler symmetric flow field. Similar adaptive procedures could be developed for the thermal and structural analysis. However, since the thermal analysis is transient the mesh would have to move with time to track the thermal response. The aerodynamic heating rate along the cylinder surface is compared with experimental results in Fig. 10(c). This new analysis approach for predicting complex flow behavior will be implemented as an alternative fluid module in LIFTS.

### Convectively Cooled Leading Edge

A 0.25 inch diameter leading edge is used in the second example to study and identify the issues related to the thermal-structural analysis and the design of convectively cooled leading edges subjected to intense aerodynamic heating. The example represents the acceleration of a hypersonic vehicle through Mach 16 which causes the vehicle nose bow shock to sweep across the engine cowl leading edge from an outboard to an inboard position. The sequence of events is classified into the three conditions shown in Fig. 11. For condition I, the oblique shock, representing the vehicle nose bow shock and created by the Mach 16 free stream flow, passes outboard of the cowl leading edge. At this condition, the cowl leading edge is exposed to the Mach 8 flow behind the Mach 16 shock wave. It should be noted that the aerodynamic heating rate on the leading edge at this Mach 8 flow (condition I) is higher than that at the Mach 16 flow (condition III) due to the additional compression of the flow as it passes through the oblique shock wave. As the vehicle continues to accelerate through Mach 16, the vehicle oblique shock wave moves across the cowl leading edge (condition II) intersecting with the leading edge bow shock to produce transient shock wave interference heating. This interference heating results in a significant amplification of the heating rate on the leading edge as shown at typical times in Fig. 12. The envelope for the peak values and the distributions are idealizations of the experimental distributions given in Ref. 16. This idealization was used because the Taylor-Galerkin explicit flow algorithm would have been prohibitively expensive to perform the analyses. The interference heating rate reaches a peak value about 22° below the horizontal centerline of the leading edge. The oblique shock is assumed to move at a speed of two inches per second and passes the leading edge in 0.125 seconds. After the oblique shock passes, the leading edge is heated by the Mach 16 flow (condition III).

The leading edge geometry, boundary conditions, and a schematic of the finite element thermal-structural model are shown in Fig. 13. The leading edge outer surface is subjected to the transient aerodynamic heating given in Fig. 12 and emits radiant energy to space. The inner surface is convectively cooled by the

direct impingement of a sonic hydrogen jet stream with an inlet temperature of 50°R. The hydrogen flow rate is 0.104 lbm/sec and the coolant film coefficient is 8 BTU/ft<sup>2</sup>s. The finite element model consists of 1440 quadrilateral elements for the leading edge and 90 mass-transport conduction/surface convection elements representing the hydrogen coolant flow. The leading edge mesh is graded in the radial direction similar to the cylinder mesh shown in Fig. 3 but is uniform in the circumferential direction. An adaptive unstructured mesh based on the temperature gradients would significantly reduce the number of grid points and elements.

Nickel-200 was first selected as the leading edge material because of its high ductility, high melting temperature, relatively low thermal expansion, and ease of fabrication. The nickel material properties used in the analysis are temperature dependent and can be found in Ref. 17. Since the structure will be brought to thermal equilibrium at condition I, the initial structural temperature was assumed to be equal to the coolant temperature of 50°R. Figure 14 shows the structure and coolant temperature histories at the selected locations shown in the inset during the sequence of events. At the early time, the leading edge is first subjected to the Mach 8 flow (condition I) for 0 s < t < 0.06 s. The figure shows that the steady-state condition is reached at the end of this time interval and the maximum temperature of about 700°R occurs at the horizontal centerline on the outer surface of the leading edge (location A). The inner surface (location B) remains at a relatively low temperature of 350°R due to heat convection to the hydrogen coolant. As the hydrogen coolant flows along the coolant passage, its temperature increases from the inlet temperature of 50°R to 77°R at the exit (location C).

During the transient interference heating (condition II, 0.06 s < t < 0.185 s), the outer surface temperature at the centerline (location A) peaks at 1500°R at the time of the oblique shock impingement (t = 0.12 s). The maximum surface temperature of approximately 2500°R occurs at 22° below the centerline (location D) due to the maximum localized heating at t = 0.14 s. The predicted peak temperature is close to the melting temperature of the nickel indicating the current design concept is not acceptable. As the oblique shock passes (t > 0.185 s), the leading edge is heated by the Mach 16 flow (condition III). The leading edge temperature drops due to the lower aerodynamic heating at this condition.

To reduce leading edge temperatures which occur during the sequence of events just described, internal fins can be added to the convectively cooled area to increase the amount of energy absorbed by the coolant. Materials with "super" thermal conductivity can be used to reduce thermal gradients through the thickness and increase circumferential diffusion of the heat load. Copper and beryllium are the candidate materials because they provide higher thermal conductivity than nickel as shown in Fig. 15. The thermal conductivity of these two materials are reported to be exceptionally high at low temperature<sup>18</sup>. The peaks of the thermal conductivity for copper and

beryllium, which occur at 20°R and 70°R, are approximately 300 and 80 times higher than nickel, respectively. However the increased conductivity occurs over a very small temperature range offering a significant challenge to the computational procedure.

The analysis is first repeated for a beryllium leading edge to investigate the reduction of the peak temperature response using a super thermal conductivity material. Internal tapered fins (~10 fins per inch) around the circumference of the leading edge are used to increase the convectively cooled area by a factor of five. However, an elementary analysis for the fin heat transfer efficiency shows that the fins increase the effective convection area by a factor of 2.5. In the analysis, the fins are taken into account by increasing the surface convection perimeter ( $P$  in eq. (5)) by a factor of 2.5. The circumferential conduction in the fin and the fin structural stiffness are not taken into account.

The beryllium leading edge temperature history for the same locations previously shown for the nickel leading edge are shown in Fig. 16. The temperature contours at the Mach 8 flow condition I and at the time of the maximum interference heating are shown in Fig. 17. Fig. 17(a) indicates that the entire leading edge acts as a super thermal conductor (illustrated by shaded area) with very low temperature rise at the Mach 8 flow condition I. As the oblique shock moves across the leading edge, the interference heating intensity increases, particularly in the shock impingement region, resulting in the localized high temperature zone shown in Fig. 17(b). This high temperature locally degrades the thermal conductivity and thus reduces the capability of conducting the high local heat flux from the leading edge outer surface to the hydrogen coolant. A maximum temperature of about 1000 °R occurs at the same time and location as for the case of the nickel leading edge. Details of the temperature response throughout the sequence of events indicate that the entire beryllium leading edge acts as a super thermal conductor at all times except during the short period of very intense aerodynamic heating shown in Fig. 17(b). No difficulties were experienced with the analysis procedure due to the extreme thermal property variation.

Since copper has a higher thermal conductivity than beryllium at temperatures above 300°R, the analysis for the copper leading edge is performed to investigate further reduction of the maximum temperature at the time of the peak aerodynamic heating. The temperature history for the same locations previously shown for the nickel and beryllium leading edges are shown in Fig. 18. The maximum temperature is reduced to 766°R. Details of the copper leading edge temperature distributions as the shock sweeps across the leading edge are shown at the selected times in Figs. 19(a)-(d). It is interesting to note that under the Mach 8 flow condition, the maximum temperature of the copper leading edge (207°R in Fig. 19(a)) is higher than the beryllium leading edge (183°R in Fig. 17(a)). This is because copper has a lower thermal conductivity than beryllium in the narrow range of temperature near 200°R.

The most severe thermal load on the copper leading edge, which occurs at the time of the peak aerodynamic heating ( $t=14$  s in Fig. 19(c)), is used in the structural analysis to study the leading edge response. Since the thermal and structural models were identical the transfer of nodal temperatures to the structural analysis was straight forward. Temperature dependent material strength properties for copper<sup>17</sup> are included in the analysis. A hydrogen coolant pressure of 1000 psi is assumed to apply uniformly along the leading edge inner surface. Along the outer surface, the aerodynamic pressure distribution is assumed to be the same shape as the aerodynamic heating<sup>16</sup> with a peak pressure of 1000 psi. These pressure distributions and the structural boundary conditions are superimposed on the predicted leading edge structural response shown in Fig. 20. The figure shows the circumferential stress distribution on the deformed leading edge. The deformed leading edge shown in this figure is greatly exaggerated to highlight the detail of the deformed shape. At the oblique shock impingement location where the peak temperature and temperature gradients occur, the deformation is 0.0005 inches and the maximum compressive stress is 25 ksi. In other regions of the leading edge, the circumferential stress is moderate varying from 10 ksi in tension to 10 ksi in compression.

The structural analysis was performed in two dimensions using the plane strain assumption. Although this is a conservative assumption, it clearly indicates the extreme axial compressive stresses (~100 ksi) that occur in the leading edge due to the extreme circumferential temperature gradient. The analysis suggests that the axial stresses for a three dimensional model of the leading edge may exceed the elastic limit of the material indicating a requirement for a nonlinear structural analysis. The current algorithm, which was derived for the inherently nonlinear fluid analysis, may be extended to three-dimensional nonlinear structural behavior with appropriate constitutive relationships. The ability to handle temperature dependent material properties and large deformations for two-dimensional problems has already been demonstrated<sup>19</sup>. The explicit algorithm with its restrictive stability criterion increases computational effort for quasi-static structural analysis, hence development of an acceleration procedure or a more efficient time marching scheme is needed.

The structural response shows that the peak circumferential stress occurs at the oblique shock impingement location where the temperature and its gradients are maximum. The very high temperature and stresses could result in the failure of the leading edge, hence a more sophisticated structural analysis may be needed to include the capability to predict the permanent localized deformation including time dependency effects, such as cyclic loading and creep, as the oblique shock moves across the leading edge. LIFTS currently has the capability for the loading part of the cycle but not the unloading. The integrated approach of the LIFTS analyzer reduced the time and effort to perform the complete fluid-thermal-structural

analysis of the leading edges. Of course, in cases of strong interdisciplinary coupling the reduction in the effort would be even more substantial.

### Concluding Remarks

A finite element approach for integrated fluid-thermal-structural analysis of aerodynamically heated leading edges was presented. The Navier-Stokes equations for high speed compressible flow and the associated thermal-structural equations were solved using a single finite element approach in one integrated, vectorized computer program called LIFTS (Langley Integrated Fluid Thermal Structural analyzer).

The approach was used to study and validate the prediction of the flow behavior and the aerothermal loads by comparing with experimental data for Mach 6.47 flow over a three inch diameter stainless steel cylinder. Comparison with experimental pressure and heat flux distributions is excellent. The thermal and structural analyses for the cylinder were performed and the response was examined to investigate benefits of the integrated interdisciplinary analysis and coupling. The coupling caused by the cylinder deformation that could alter the flow field was negligible. The fluid-thermal coupling from the increase in the cylinder temperature, which results in a reduction of the aerodynamic heating, was moderate but significant. The procedure automatically applies the true interface conditions (boundary conditions in a non-integrated procedure) as the solution is marched in time, thus avoiding the time and effort to interpolate data between different disciplinary models. The aerodynamic heating using the explicit Taylor-Galerkin algorithm converged very slowly because of the small time steps required for computational stability. Adaptive unstructured remeshing is required to reduce the computational effort. A new approach with a more efficient aerodynamic fluid algorithm and adaptive unstructured remeshing was described and will be incorporated into LIFTS as an alternative approach for the fluid analysis.

Critical issues for the thermal-structural analysis were demonstrated by the analyses of a hydrogen cooled leading edge subjected to intense aerodynamic heating. The use of super thermal conductivity materials alleviates the elevated leading edge temperatures and gradients and hence the stress levels. The approach clearly demonstrates the ability to perform transient nonlinear thermal analysis for problems with highly nonlinear temperature dependent material properties and various boundary conditions. Under severe aerothermal loads which can cause intense localized leading edge temperatures, the present analysis indicates the need for more efficient algorithm with capability to predict the nonlinear, time dependent structural response.

The applications have demonstrated the fundamental capability of the integrated analysis approach and provided insight into the features of the hypersonic flow over the leading edge, the leading edge thermal-structural response, and their interactions. Future analyses will study the flow-

thermal-structural interactions for a more complex flow field that is altered by a larger structural deformation to further demonstrate the applicability and benefits of the approach for coupled interdisciplinary problems.

### References

1. Shideler, J. L., Webb, G. L. and Pittman, C. M.: "Verification Tests of Durable Thermal Protection System Concepts," *Journal of Spacecraft and Rockets*, Vol. 22, No. 6, November 1985, pp. 598-604.
2. Olsen, G. C., and Smith, R. E.: "Analysis of Aerothermal Loads on Spherical Dome Protuberances," *AIAA Journal*, Vol. 23, No. 5, May 1985, pp. 650-656.
3. Glass, C. E. and Hunt, L. R.: "Aerothermal Tests of Spherical Dome Protuberance on a Flat Plate at a Mach Number of 6.5," NASA Technical Paper 2631, December 1986.
4. Thornton, E. A. and Dechaumphai, P.: "Coupled Flow, Thermal and Structural Analysis of Aerodynamically Heated Panels," Presented at the AIAA/ASME/AHS 28th Structures, Structural Dynamics and Materials Conference, Monterey, California, April 6-8, 1987, AIAA Paper No. 87-0701.
5. Thornton, E. A. and Dechaumphai, P.: "Finite Element Prediction of Aerothermal-Structural Interaction of Aerodynamically Heated Panels," Presented at the AIAA 22nd Thermophysics Conference, Honolulu, Hawaii, June 8-10, 1987 AIAA Paper No. 87-1610.
6. Wieting, A. R.: "Experimental Study of Shock Wave Interference Heating on a Cylindrical Leading Edge," Ph.D. Dissertation, Old Dominion University, Norfolk, Virginia, 1987, also NASA TM-100484, 1987.
7. White, F. M.: *Viscous Fluid Flow*, McGraw-Hill, 1974.
8. Thornton, E. A. and Wieting, A. R.: "Finite Element Methodology for Transient Conduction/Forced Convection Thermal Analysis," *Progress in Astronautics and Aeronautics: Heat Transfer, Thermal Control and Heat Pipes*, Vol. 70, Edited by Walter B. Olstad, AIAA, New York, pp. 77-103.
9. Bey, K. S., Thornton, E. A., Dechaumphai, P. and Ramakrishnan, R.: "A New Finite Element Approach for Prediction of Aerothermal Loads - Progress in Inviscid Flow Computations," Presented at the AIAA 7th Computational Fluid Dynamics Conference, Cincinnati, Ohio, July 15-17, 1985, AIAA Paper No. 85-1533, also NASA TM 86434.
10. Thornton, E. A. and Dechaumphai, P.: "A Taylor-Galerkin Finite Element Algorithm for Transient Nonlinear Thermal-Structural Analysis,"

Presented at the AIAA/ASME/AHS 27th Structures, Structural Dynamics and Materials Conference, San Antonio, Texas, May 19-21, 1986, AIAA Paper No. 86-0911.

11. Thornton, E. A., Dechaumphai, P. and Vermaganti, G.: "A Finite Element Approach for Prediction of Aerostructural Loads," Presented at the AIAA/ASME 4th Joint Fluid Mechanics, Plasma Dynamics and Laser Conference, Atlanta, Georgia, May 12-14, 1986, AIAA Paper No. 86-1050.
12. Billig, F. S.: "Shock-Wave Shapes Around Spherical and Cylindrical Nosed Bodies," *Journal of Spacecraft and Rockets*, Vol. 4, No. 6, June 1967, pp. 822-823.
13. Fay, J. A. and Riddell, F. R.: "Theory of Stagnation Point Heat Transfer in Dissociated Air," *Journal of the Aeronautic Sciences*, Vol. 25, No. 2, February 1958, pp. 73-85.
14. Holcomb, J. E., Curtis, J. T., Shope, F. L.: "A New Version of the CVEQ Hemisphere Viscous Shock Layer Program for Equilibrium Air," AEDC-TMR-85-V7, February 1985.
15. Thareja, R. R., Stewart, J. R., Hassan, O., Morgan, K., and Peraire, J.: "A Point Implicit Unstructured Grid Solver for the Euler and Navier-Stokes Equations," Presented at the AIAA 26th Aerospace Sciences Meeting, Reno, Nevada, January 11-14, 1988, AIAA Paper No. 88-0036.
16. Holden, M. S., and Wieting, A. R., Moselle, J. R., and Glass, C.: "Studies of Aerostructural Loads Generated in Regions of Shock/Shock Interaction in Hypersonic Flow," Presented at the AIAA 26th Aerospace Sciences Meeting, Reno, Nevada, January 11-14, 1988, AIAA Paper No. 88-0477.
17. Metals Handbook Committee: *Metals Handbook*, Eighth Edition, American Society for Metals, Ohio, 1975.
18. Touloukian, Y. S., Powell, R. W., Ho, C. Y., and Klømens, P. G.: "Thermal Conductivity for Metallic Elements and Alloys," *Thermophysical Properties of Matter*, Vol. 1, IFI/Plenum, New York, 1970.
19. Dechaumphai, P., Wieting, A. R., and Thornton, E. A.: "Thermal Structural Performance of an Actively Cooled Leading Edge Subjected to Type IV Shock Wave Interference Heating," Third National Aero-Space Plane Symposium June 2-4, 1987, Paper No. 24.

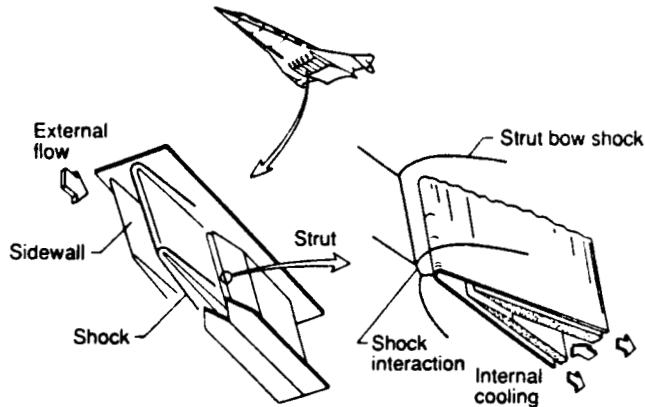


Fig. 1 Fluid-thermal-structural interactions on an aerospace plane scramjet engine leading edge.

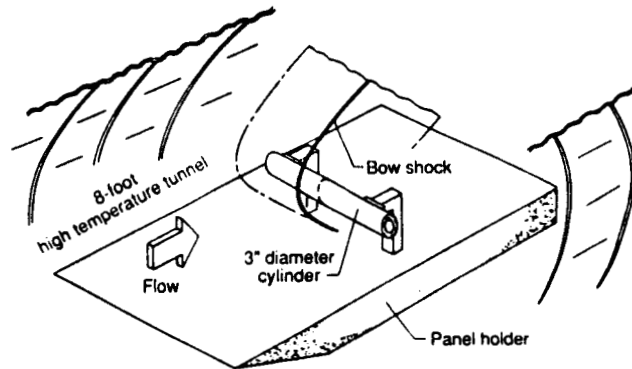


Fig. 2 Experimental configuration for flow over a three inch diameter cylinder in the 8-Foot High Temperature Tunnel.

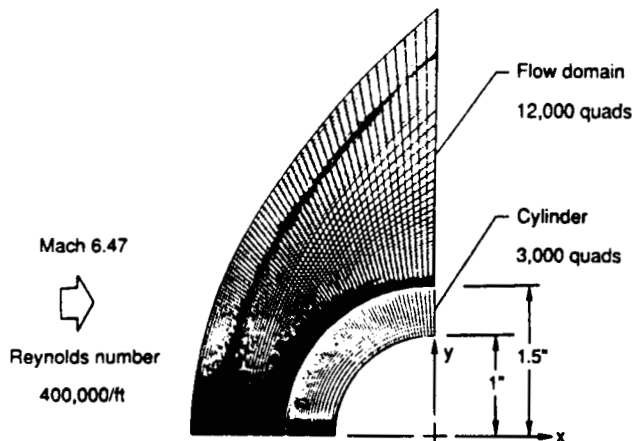


Fig. 3 Fluid-thermal-structural finite element model for flow over a three inch diameter cylinder.

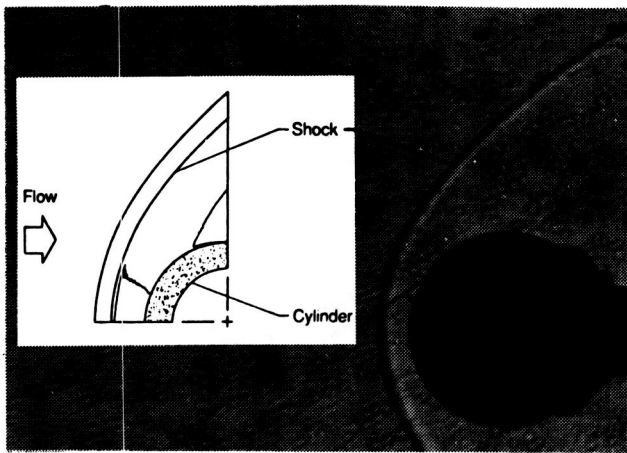


Fig. 4 Comparison of density contours with Schlieren photograph for Mach 6.47 flow over a three inch diameter cylinder.

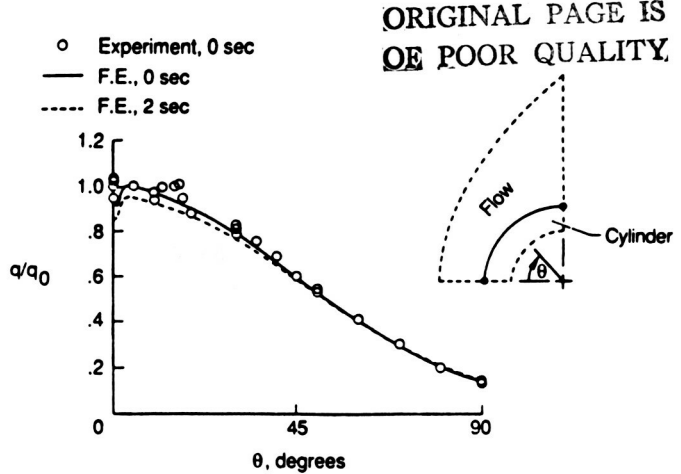


Fig. 7 Comparative surface heating rate distributions on a three inch diameter cylinder subjected to Mach 6.47 flow.

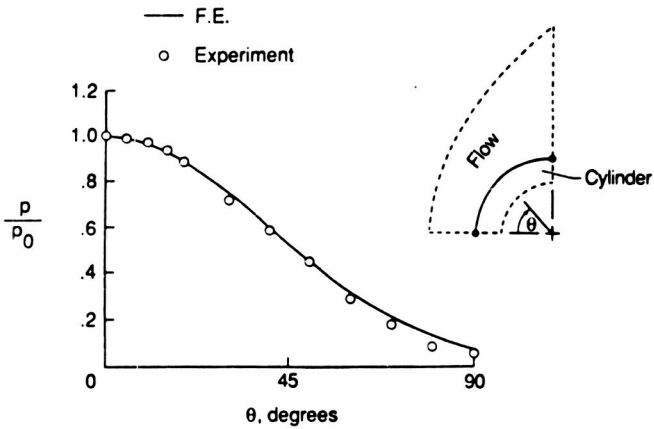


Fig. 5 Comparative surface pressure distributions on a three inch diameter cylinder subjected to Mach 6.47 flow.

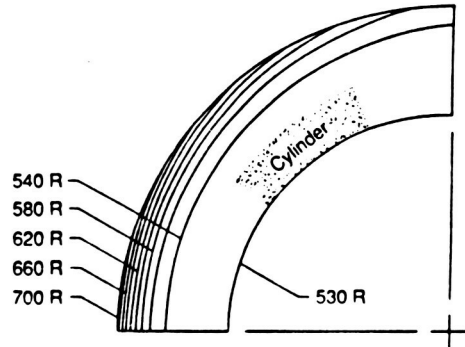


Fig. 8 Temperature contours on a three inch diameter cylinder at 2 seconds.

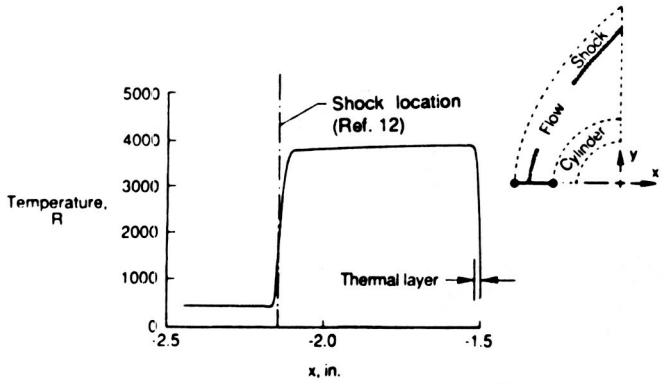


Fig. 6 Fluid temperature distribution along the centerline of a three inch diameter cylinder for Mach 6.47 flow.

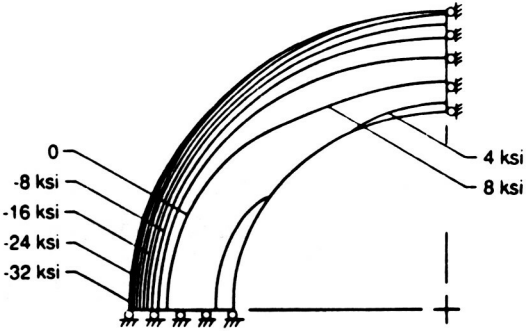
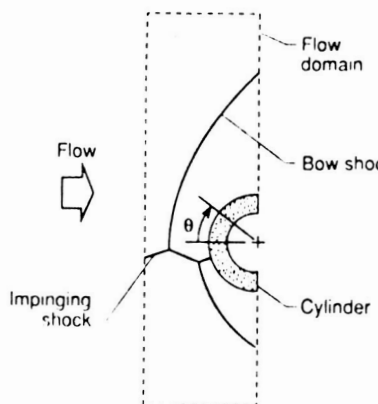


Fig. 9 Circumferential stress contours on a three inch diameter cylinder at 2 seconds.



a) Oblique shock and bow shock interaction on cylinder.

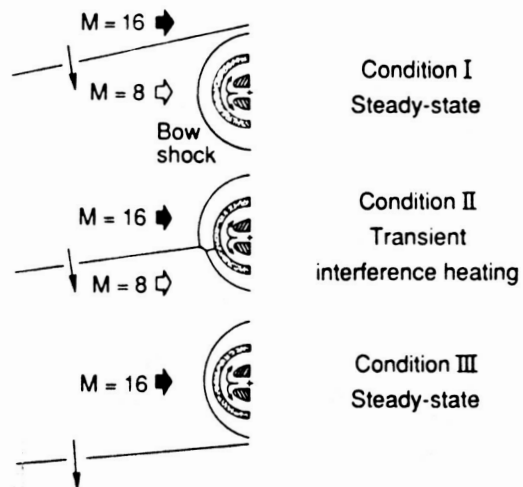
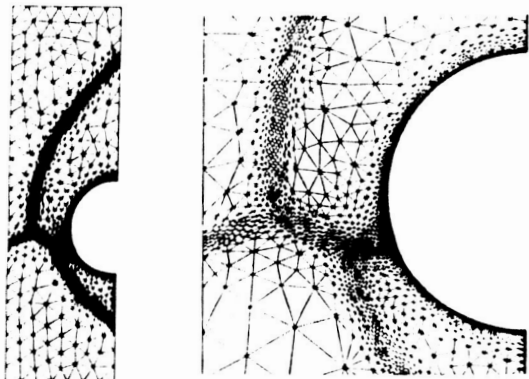
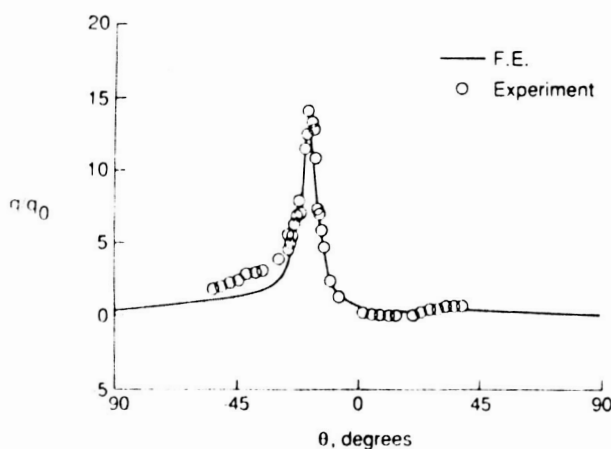


Fig. 11 A 0.25 inch diameter hydrogen cooled leading edge with shock wave interference heating.



b) Adaptive mesh with enlarged section.



c) Comparative surface heating rate distribution.

Fig. 10 Adaptive mesh refinement flow model and aerodynamic heating for cylinder with impinging oblique shock and bow shock interaction.

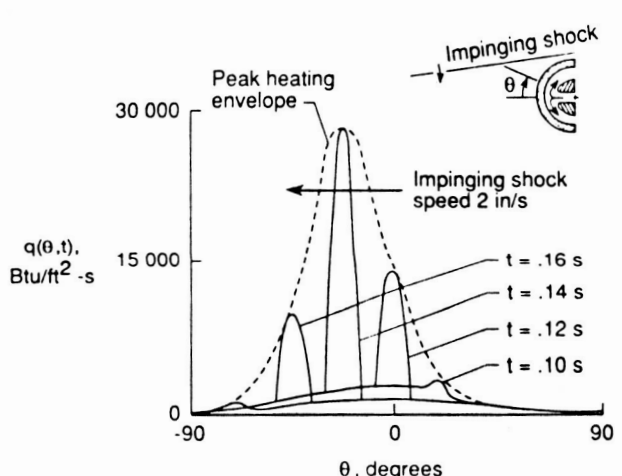


Fig. 12 Leading edge transient interference heating due to vehicle acceleration at Mach 16.

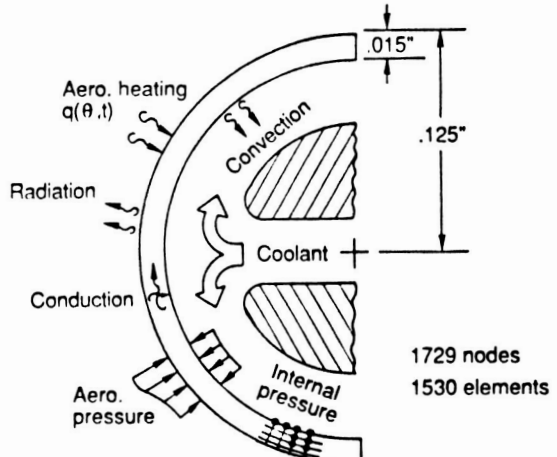


Fig. 13 A schematic thermal-structural finite element model of 0.25 inch diameter leading edge with boundary conditions.

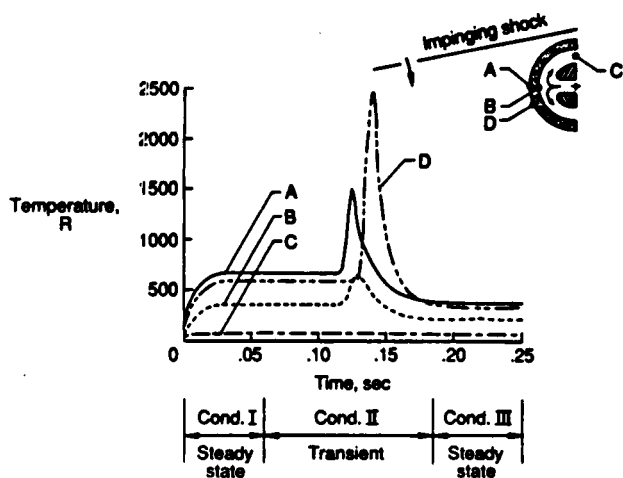


Fig. 14 Nickel leading edge temperature response.

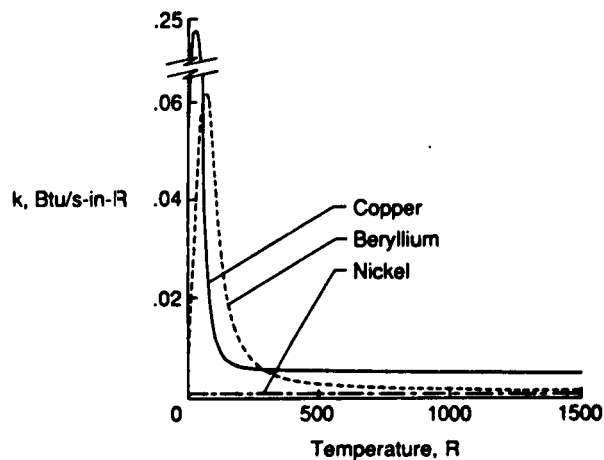
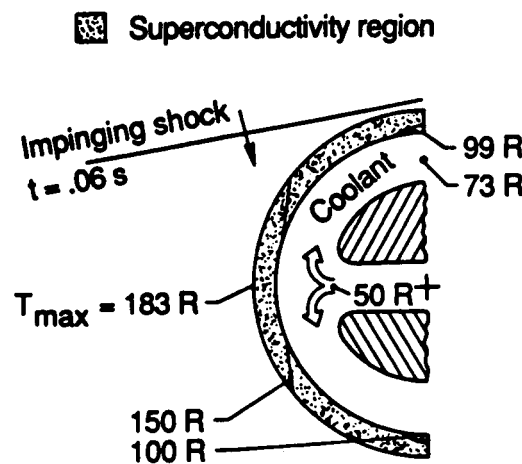
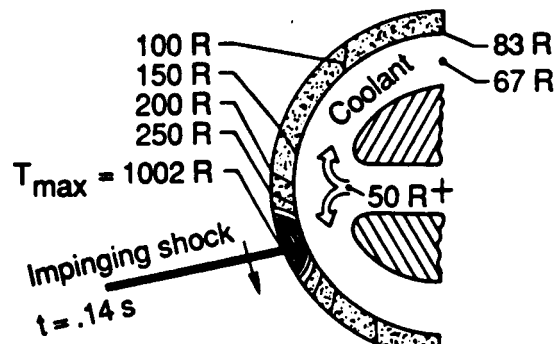


Fig. 15 Temperature dependent thermal conductivity for copper, beryllium, and nickel.



a) Mach 8 flow.



b) Maximum interference heating.

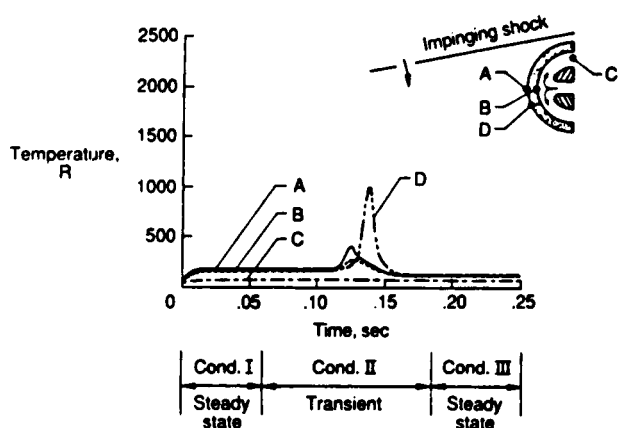


Fig. 16 Beryllium leading edge temperature response.

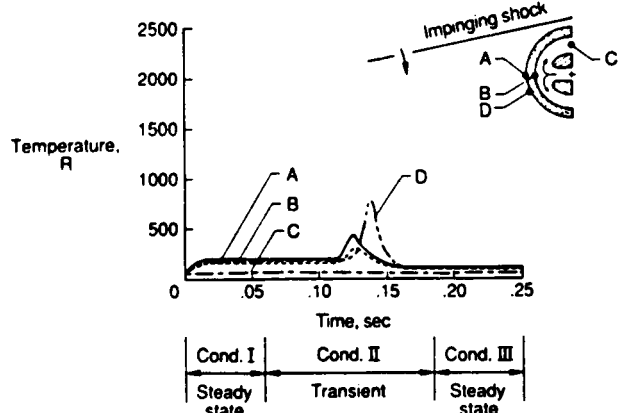
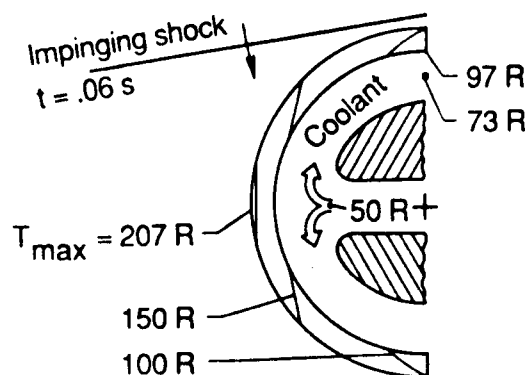
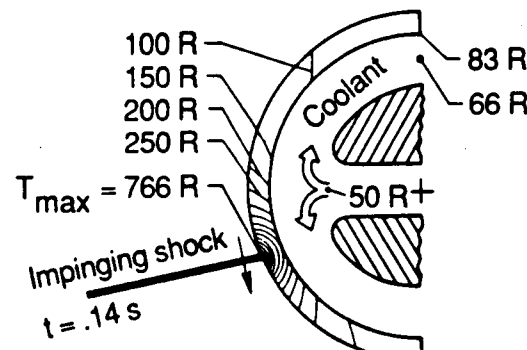


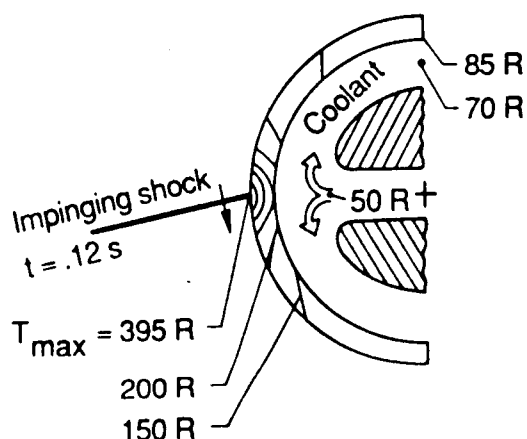
Fig. 18 Copper leading edge temperature response.



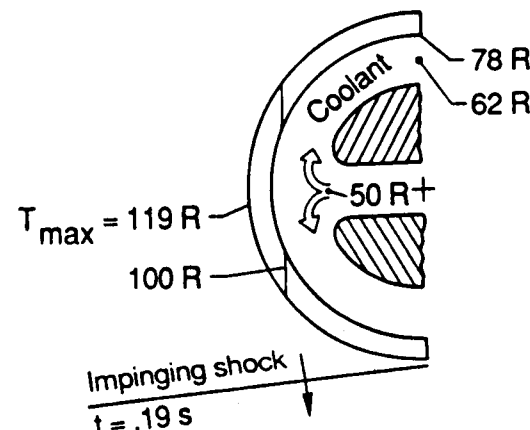
a) Mach 8 flow.



c) Maximum interference heating.



b) Interference heating.



d) Mach 16 flow.

Fig. 19 Temperature contours for copper leading edge.

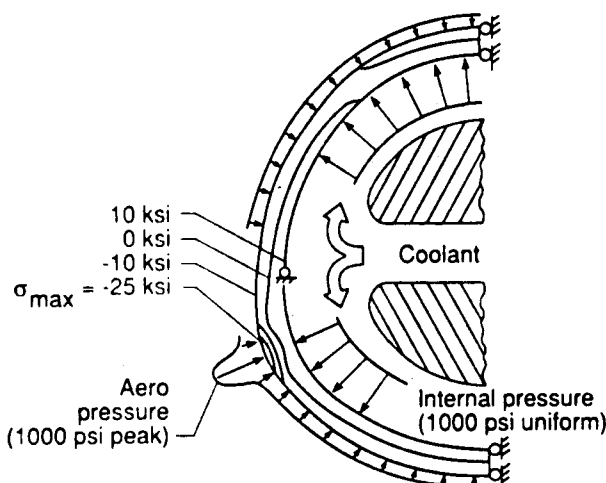


Fig. 20 Loads and circumferential stress contours on deformed copper leading edge at maximum interference heating.



National Aeronautics and

Space Administration

## Report Documentation Page

1. Report No. <i>NASA TM-100579</i>	2. Government Accession No.	3. Recipient's Catalog No.	
4. Title and Subtitle <i>Fluid-Thermal-Structural Study of Aerodynamically Heated Leading Edges</i>		5. Report Date <i>April 1988</i>	
		6. Performing Organization Code	
7. Author(s) <i>Pramote Dechaumphai, Earl A. Thornton, and Allan R. Wieting</i>		8. Performing Organization Report No.	
		10. Work Unit No. <i>506-43-31-03</i>	
9. Performing Organization Name and Address <i>Langley Research Center Hampton, VA 23665-5225</i>		11. Contract or Grant No.	
		13. Type of Report and Period Covered <i>Technical Memorandum</i>	
12. Sponsoring Agency Name and Address <i>National Aeronautics and Space Administration Washington, DC 20546</i>		14. Sponsoring Agency Code	
15. Supplementary Notes <i>Pramote Dechaumphai, and Allan Wieting, Langley Research Center; Earl Thornton, Old Dominion University. Presented to AIAA/ASME/ASCE/AHS 29th Structures, Structural Dynamics and Materials Conference, Williamsburg, VA, April 18-20, 1988.</i>			
16. Abstract <i>A finite element approach for integrated fluid-thermal-structural analysis of aerodynamically heated leading edges is presented. The Navier-Stokes equations for high speed compressible flow, the energy equation, and the quasi-static equilibrium equations for the leading edge are solved using a single finite element approach in one integrated, vectorized computer program called LIFTS. The fluid-thermal-structural coupling is studied for Mach 6.47 flow over a 3-inch diameter cylinder for which the flow behavior and the aero thermal loads are calibrated by experimental data. Issues of the thermal-structural response are studied for hydrogen cooled, super thermal conducting leading edges subjected to intense aerodynamic heating.</i>			
17. Key Words (Suggested by Author(s)) <i>High Speed Flows Aerodynamic Heating Thermal Stress Finite Element</i>		18. Distribution Statement <i>Unclassified - Unlimited Subject Category 39</i>	
19. Security Classif. (of this report) <i>Unclassified</i>	20. Security Classif. (of this page) <i>Unclassified</i>	21. No. of pages <i>15</i>	22. Price <i>A02</i>